Received: 11 September 2023 | Accepted: 20 November 2023
DOI: 10.1002/gamm.202370010

ORIGINAL ARTICLE

GAMM Mitteilungen

Numerical evaluation of elasto-mechanical and visco-elastic electro-mechanical models of the human heart

Jonathan Fröhlich[1] | **Tobias Gerach**[2] | **Jonathan Krauß**[2] | **Axel Loewe**[2] |
Laura Stengel[1] | **Christian Wieners**[1]

[1]Institute of Applied and Numerical Mathematics, Karlsruhe Institute of Technology (KIT), Baden-Württemberg, Germany

[2]Institute of Biomedical Engineering, Karlsruhe Institute of Technology (KIT), Baden-Württemberg, Germany

Correspondence
Christian Wieners, Institute of Applied and Numerical Mathematics, Karlsruhe Institute of Technology (KIT), Baden-Württemberg, Germany.
Email: christian.wieners@kit.edu

Funding information
Deutsche Forschung gemeinschaft (DFG, German Research Foundation), Grant/Award Numbers: 465189069(SPP2311), 258734477(CRC1173)

Abstract

We investigate the properties of static mechanical and dynamic electro-mechanical models for the deformation of the human heart. Numerically this is realized by a staggered scheme for the coupled partial/ordinary differential equation (PDE-ODE) system. First, we consider a static and purely mechanical benchmark configuration on a realistic geometry of the human ventricles. Using a penalty term for quasi-incompressibility, we test different parameters and mesh sizes and observe that this approach is not sufficient for lowest order conforming finite elements. Then, we compare the approaches of active stress and active strain for cardiac muscle contraction. Finally, we compare in a coupled anatomically realistic electro-mechanical model numerical Newmark damping with a visco-elastic model using Rayleigh damping. Nonphysiological oscillations can be better mitigated using viscosity.

KEYWORDS
convergence analysis, electro-mechanical cardiac modeling, Newmark damping, quasi-incompressible mechanical models, visco-elasticity

1 | INTRODUCTION

Computational modeling and simulation of the cardiovascular system has significantly advanced in the recent decades [26, 30] and successfully translated to clinical impact in the realms of diagnosis [3], risk stratification [4], therapy planning [24, 32], and intraprocedural support [22]. An overview on mathematical models and numerical methods is given in [33].

Our goal is to investigate the impact of both modeling and numerical decisions when solving coupled cardiac systems. We hypothesize that the errors introduced by the respective decisions can be distinguished: Modeling errors should be visible qualitatively, while numerical errors dominate the solution for coarse simulations.

Computational models are often limited to a single function ("physics") of the cardiovascular system such as electrophysiology, solid biomechanics, blood flow in the heart or the circulatory system. These single-physics approaches are very valuable research tools for cardiac diseases that are mostly confined to a single function. As an example, typical forms of arrhythmia can be explained, diagnosed and treated purely electrophysiologically. However, single-physics models are of limited value to eventually improve patient care for complex diseases involving several functions of the heart. Therefore, multiphysics approaches of high biophysical fidelity are required to empower and qualify computational methods as a valuable complementary research tool contributing to tackle complex diseases.

The copyright line for this article was changed on 22 February 2024 after original online publication.

In [14] and [9], a fully coupled multiscale model of the human heart is realized including all four chambers and the "physics" electrophysiology, mechanics, and a closed-loop circulation. Together with the computational models developed in [12, 13, 18], this builds the basis for this contribution. To describe the tissue mechanics, we use the transversely isotropic constitutive law by Guccione [16], which depends on the preferential myocyte direction, also known as fiber direction, in the cardiac tissue.

Here, we restrict ourselves to an anatomically accurate model of the human ventricles, described by a tetrahedral mesh in the unloaded reference configuration to study the mechanical properties of the system in detail. For all tests, we use lowest-order conforming finite elements for the partial differential equations (PDEs) and element-wise constant approximations for the ordinary differential equations (ODEs). We test the convergence of the approximation by comparing the results on different spatiotemporal refinement levels.

Our main goal is to investigate the properties of the cardiac mechanics solution depending on different model variants and parameters. In addition, we compare the results for different resolutions of the discretization in space and time.

The remainder of the manuscript is organized as follows. We start by defining the model to be used, followed by an explanation of the discretization and solution schemes. Then, the following mechanical properties are investigated:

- In the first numerical experiment, we test the convergence of the initial configuration of the cardiac cycle, where the blood pressure in the ventricles results into a finite elasticity problem with nonlinear Neumann boundary conditions.
- Then, we transfer the setting from the benchmark problem proposed by Land et al. [21], that is, from a simple ellipsoid, to a more realistic biventricular configuration. Here, we compare the active strain and active stress approaches for the contraction of the heart muscle [1, 2, 28, 29, 36]. We are interested in determining whether there are substantial differences between the two active deformation approaches or if similar results can be achieved.
- For the dynamic electro-mechanical model, we compare numerical damping by the Newmark time-stepping scheme with a physical model using Rayleigh damping. For the electrophysiology, we are using the ten Tusscher et al. cell model. We especially seek to answer if modeling of a physical damping is necessary within realistic cardiac simulations.

We conclude with a short discussion of our observations and of possible extensions of the presented electro-mechanical investigations.

2 | A COUPLED ELECTRO-MECHANICAL MODEL FOR THE HEART

Let $\Omega \subset \mathbb{R}^3$ be a bounded Lipschitz domain describing the unloaded reference geometry of the heart (see [35, Sect. 2.6] for details on how to obtain the reference geometry from tomographic imaging data). Let $\Omega_{\mathrm{EP}} \subset \Omega$ be the subdomain where the cardiac electrophysiology is active, that is, the myocardium. In Ω, we compute the displacement $\boldsymbol{u}$ defining the deformation $\boldsymbol{\varphi}(t,\boldsymbol{x}) = \boldsymbol{x} + \boldsymbol{u}(t,\boldsymbol{x})$ of the heart, and $\Omega^{\boldsymbol{\varphi}} = \boldsymbol{\varphi}(\Omega)$ is the deformed geometry. The deformation gradient is denoted by $\boldsymbol{F} = \mathrm{D}\boldsymbol{\varphi} = \boldsymbol{I} + \mathrm{D}\boldsymbol{u}$, the local volume change is given by the Jacobian $J = \det \boldsymbol{F}$, the velocity is $\boldsymbol{v} = \partial_t \boldsymbol{u}$, and its gradient is $\dot{\boldsymbol{F}} = \mathrm{D}\boldsymbol{v}$. The direction of the cardiac fibers in the reference geometry Ω is denoted by $\boldsymbol{f}$ with $|\boldsymbol{f}| = 1$. The contraction of the heart is activated by the fiber stretch $\gamma_{\boldsymbol{f}}$. The stretch is a result of the active tension developed in the myocytes in response to the calcium dynamics inside the cell governed by the electrophysiology model in Ω_{EP}, mainly determined by the difference between the intracellular and extracellular electric potential v_{m} and the vectors of ion concentrations $\boldsymbol{c}$ and gating variables $\boldsymbol{w}$.

We study the PDE-ODE system for $(v_{\mathrm{m}}, \boldsymbol{c}, \boldsymbol{w}, \boldsymbol{\varphi}, \gamma_{\boldsymbol{f}})$ describing the heart's function during a cardiac cycle $(0, T)$

$$
\begin{aligned}
\beta_{\mathrm{sv}} C_{\mathrm{m}} \partial_t \left(J v_{\mathrm{m}}\right) &= \nabla \cdot \left(\boldsymbol{D}^{\boldsymbol{\varphi}} \nabla v_{\mathrm{m}}\right) - J\left(\beta_{\mathrm{sv}} I_{\mathrm{ion}}(v_{\mathrm{m}}, \boldsymbol{c}, \boldsymbol{w}) - \beta_{\mathrm{sv}} I_{\mathrm{ext}}\right) && \text{in } \Omega_{\mathrm{EP}}, && \text{(1a)}\\
\partial_t \boldsymbol{c} &= \boldsymbol{G}_{\boldsymbol{c}}(v_{\mathrm{m}}, \boldsymbol{c}, \boldsymbol{w}) && \text{in } \Omega_{\mathrm{EP}}, && \text{(1b)}\\
\partial_t \boldsymbol{w} &= \boldsymbol{G}_{\boldsymbol{w}}(v_{\mathrm{m}}, \boldsymbol{c}, \boldsymbol{w}) && \text{in } \Omega_{\mathrm{EP}}, && \text{(1c)}\\
\rho\left(\partial_t^2 \boldsymbol{\varphi} + \alpha_{\mathrm{R}} \partial_t \boldsymbol{\varphi}\right) &= \operatorname{div} \boldsymbol{P}_{\mathrm{eff}}\left(\boldsymbol{F}, \dot{\boldsymbol{F}}, \boldsymbol{f}, \gamma_{\boldsymbol{f}}\right) && \text{in } \Omega, && \text{(1d)}\\
\partial_t \gamma_{\boldsymbol{f}} &= G_{\gamma_{\boldsymbol{f}}}(\gamma_{\boldsymbol{f}}, \boldsymbol{F}, \boldsymbol{f}, \boldsymbol{c}) && \text{in } \Omega_{\mathrm{EP}}. && \text{(1e)}
\end{aligned}
$$

The parabolic equation (1a) for the transmembrane voltage v_{m} depends on the surface-to-volume ratio β_{sv}, the membrane capacitance C_{m}, the symmetric anisotropic conductivity tensor $\boldsymbol{D}_0$ depending on the fiber direction $\boldsymbol{f}$, the ionic transmembrane current I_{ion} and the external current I_{ext} modeling the electric activation. The equations in the deformed geometry $\Omega_{\mathrm{EP}}^{\boldsymbol{\varphi}}$ are computed in the reference geometry Ω_{EP}, so that we need to transform the conductivity tensor to the deformed geometry by $\boldsymbol{D}^{\boldsymbol{\varphi}} = J\boldsymbol{F}^{-1}\boldsymbol{D}_0\boldsymbol{F}^{-\top}$, and potential and currents are scaled with the volume change of the deformation J, compare [2, Eqn. (2.8)].

The concentrations and gating variables are determined by a coupled ODE system (1b) and (1c) determined by $\boldsymbol{G_c}$ and $\boldsymbol{G_w}$ depending on the transmembrane voltage, the ion concentrations and the gating variables. In our tests, we use the ten Tusscher et al. ionic model [41] for $\boldsymbol{G_c}$, $\boldsymbol{G_w}$ and I_{ion}, and the activation pattern defined in [23] for I_{ext}.

The elasto-dynamic cardiac deformation is determined by (1d), where ρ is the material density, $\boldsymbol{P}_{\mathrm{eff}}$ is the effective activated stress in the deformed configuration combining the Piola–Kirchhoff stress $\boldsymbol{P}$ with the active stress or strain, and α_{R} is the Rayleigh damping parameter. Here, we utilize the reduced version of the Rayleigh damping as described in [20], and the hyperelastic transversely isotropic constitutive law by Guccione et al. [16]

$$\widehat{W}_{\mathrm{Gucc}}(\boldsymbol{E},\boldsymbol{f}) = \frac{1}{2}C_{\mathrm{Gucc}}\left(\exp(Q(\boldsymbol{E},\boldsymbol{f})) - 1\right) \ , \qquad Q(\boldsymbol{E},\boldsymbol{f}) = 4c_1(\boldsymbol{f}\cdot\boldsymbol{E}\boldsymbol{f})^2 + 4c_2(\boldsymbol{E}\boldsymbol{f}\cdot\boldsymbol{E}\boldsymbol{f}) + 4c_3(\boldsymbol{E}:\boldsymbol{E}) \tag{2}$$

depending on the Green–Lagrange strain tensor $\boldsymbol{E} = \frac{1}{2}(\boldsymbol{F}^{\top}\boldsymbol{F} - \boldsymbol{I})$, the fiber direction $\boldsymbol{f}$ in the reference configuration, and parameters $C_{\mathrm{Gucc}}, b_{\boldsymbol{f}}, b_{\boldsymbol{f},\boldsymbol{s}}, b_{\boldsymbol{s}}$ defining $c_1 = \dfrac{1}{4}(b_{\boldsymbol{f}} - 2b_{\boldsymbol{f},\boldsymbol{s}} + b_{\boldsymbol{s}})$, $c_2 = \dfrac{1}{2}(b_{\boldsymbol{f},\boldsymbol{s}} - b_{\boldsymbol{s}})$, and $c_3 = \dfrac{1}{4}b_{\boldsymbol{s}}$. Combined with a volumetric penalty $\kappa_{\mathrm{vol}} > 0$ to approximate incompressibility, we obtain the elastic potential

$$\widehat{W}(\boldsymbol{E},\boldsymbol{f},J) = \widehat{W}_{\mathrm{Gucc}}(\boldsymbol{E},\boldsymbol{f}) + \kappa_{\mathrm{vol}}W_{\mathrm{vol}}(J) \ , \qquad W_{\mathrm{vol}}(J) = \frac{1}{2}(J-1)^2 \ . \tag{3}$$

The effective stress in case of the active strain model [28], [33, Eqn. (6.28)] is given in the reference configuration by

$$\boldsymbol{P}_{\mathrm{eff}}\left(\boldsymbol{F},\dot{\boldsymbol{F}},\boldsymbol{f},\gamma_{\boldsymbol{f}}\right) = \boldsymbol{P}\left(\boldsymbol{F}\boldsymbol{F}_{\mathrm{a}}^{-1},\dot{\boldsymbol{E}},\boldsymbol{f}\right) \ , \quad \boldsymbol{P}\left(\boldsymbol{F}_{\mathrm{eff}},\dot{\boldsymbol{E}},\boldsymbol{f}\right) = \boldsymbol{F}_{\mathrm{eff}}\mathrm{D}_{\boldsymbol{E}}\widehat{W}_{\mathrm{Gucc}}(\boldsymbol{E}_{\mathrm{eff}},\boldsymbol{f}) + \kappa_{\mathrm{vol}}\mathrm{D}_{\boldsymbol{F}}W_{\mathrm{vol}}(\det\boldsymbol{F}_{\mathrm{eff}}), \tag{4}$$

with $\boldsymbol{F}_{\mathrm{eff}} = \boldsymbol{F}\boldsymbol{F}_{\mathrm{a}}^{-1}$ and the active strain $\boldsymbol{F}_{\mathrm{a}}$ depending on the fiber stretch $\gamma_{\boldsymbol{f}}$

$$\boldsymbol{F}_{\mathrm{a}} = \begin{cases} (1+\gamma_{\boldsymbol{f}})\boldsymbol{f}\boldsymbol{f}^{\top} + \frac{1}{\sqrt{1+\gamma_{\boldsymbol{f}}}}\left(\boldsymbol{I} - \boldsymbol{f}\boldsymbol{f}^{\top}\right), & \text{if } 1+\gamma_{\boldsymbol{f}} > 0, \\ \boldsymbol{I}, & \text{else.} \end{cases} \tag{5}$$

The active stress model [1], [33, Eqn. (6.23)] is defined by

$$\boldsymbol{P}_{\mathrm{eff}}\left(\boldsymbol{F},\dot{\boldsymbol{F}},\boldsymbol{f},\gamma_{\boldsymbol{f}}\right) = \boldsymbol{F}\left(\mathrm{D}_{\boldsymbol{E}}\widehat{W}_{\mathrm{Gucc}}(\boldsymbol{E},\boldsymbol{f}) + T_{\mathrm{a}}\boldsymbol{f}\boldsymbol{f}^{\top}\right) + \kappa_{\mathrm{vol}}\mathrm{D}_{\boldsymbol{F}}\widehat{W}_{\mathrm{vol}}(\det\boldsymbol{F}) \ , \tag{6}$$

where the active stress is given by $T_{\mathrm{a}}\boldsymbol{f}\boldsymbol{f}^{\top}$ depending on the chosen model for T_{a} [15]. Typically, T_{a} is computed based on the intracellular calcium concentration and the fiber stretch $\gamma_{\boldsymbol{f}}$.

The contraction of the heart is initiated by an increase of the ionic concentration and the resulting fiber stretch is computed by the ODE (1e) determined by $G_{\gamma_{\boldsymbol{f}}}$. We use the stretch model introduced by Rossi et al. [37]: denoting the 4th invariant along $\boldsymbol{f}$ by $\iota_{4,\boldsymbol{f}}(\boldsymbol{F}) = (\boldsymbol{F}\boldsymbol{f})\cdot(\boldsymbol{F}\boldsymbol{f})$, the evolution of $\gamma_{\boldsymbol{f}}$ is of the form $G_{\gamma_{\boldsymbol{f}}}(\gamma_{\boldsymbol{f}},\boldsymbol{F},\boldsymbol{f},\boldsymbol{c}) = g_{\gamma_{\boldsymbol{f}}}(\gamma_{\boldsymbol{f}},\iota_{4,\boldsymbol{f}}(\boldsymbol{F}),\boldsymbol{f},c_{\mathrm{Ca}})$ with

$$g_{\gamma_{\boldsymbol{f}}}(\gamma_{\boldsymbol{f}},\iota_{4,\boldsymbol{f}}(\boldsymbol{F}),\boldsymbol{f},c_{\mathrm{Ca}}) = \frac{1}{\mu_{\boldsymbol{f}}c_{\mathrm{Ca}}^2}\left(\alpha_{\boldsymbol{f}}f_{\boldsymbol{k}}(c_{\mathrm{Ca}})R_{\mathrm{FL}}(\ell_{\mathrm{R},0}\iota_{4,\boldsymbol{f}}) + \iota_{4,\boldsymbol{f}}\sum_{j=1}^{5}(-1)^j(j+1)(j+2)\gamma_{\boldsymbol{f}}^j\right), \tag{7}$$

where $f_{\boldsymbol{k}}(c_{\mathrm{Ca}}) = \left(c_{\mathrm{Ca}} - c_{\mathrm{Ca},0}\right)^2$ is the active tension generated by the contractile force of the sarcomere, $\ell_{\mathrm{R},0}$ is the initial sarcomere length and

$$R_{\mathrm{FL}}(\ell_{\mathrm{R}}) = \begin{cases} \dfrac{c_0^{\mathrm{FL}}}{2} + \sum_{k=1}^{3}\left(c_k^{\mathrm{FL}}\sin(k\ell_{\mathrm{R}}) + d_k^{\mathrm{FL}}\cos(k\ell_{\mathrm{R}})\right), & \ell_{\mathrm{R}} \in [\ell_{\mathrm{R,min}},\ell_{\mathrm{R,max}}], \\ 0, & \text{else,} \end{cases}$$

is the force–length relationship depending on $\ell_{\mathrm{R}} = \ell_{\mathrm{R},0}\iota_{4,\boldsymbol{f}}$.

The coupled PDE-ODE model is complemented with initial conditions and boundary conditions on the endocardial wall $\Gamma_{\mathrm{C}} \subset \partial\Omega$ and on the pericardium $\Gamma_{\mathrm{P}} \subset \partial\Omega$, as well as Dirichlet boundary conditions on $\Gamma_{\mathrm{D}} = \partial\Omega \setminus \partial\Omega_{\mathrm{EP}}$.

For simplicity, we use homogeneous Dirichlet boundary conditions for the displacement on Γ_{D} and homogeneous Neumann boundary conditions on Γ_{P} for the numerical tests in this work. On the endocardial wall, we apply a pressure load

$$\boldsymbol{P}_{\mathrm{eff}}\boldsymbol{n} = -p_{\mathrm{C}} Cof(\boldsymbol{F})\boldsymbol{n} \qquad \text{on } \Gamma_{\mathrm{C}} \ ,$$

where $\boldsymbol{n}$ is the unit outer normal vector on the boundary of the reference domain $\partial\Omega$.

For a full closed-loop model, a coupling to the circulatory system is required, which can be approximated by an additional ODE system coupled to the PDE-ODE system (1) by the pressure in the cardiac chambers and their volumes. For more details we refer to [9, 11, 14, 25, 34]. Realistic boundary conditions at the pericardium are given by a free-slip mortar setting [11]. Alternatively, they can be approximated by normal penalty conditions [9, 31, 40].

3 | A STAGGERED NUMERICAL APPROXIMATION SCHEME

Let $\Omega_h = \bigcup_{K\in\mathcal{K}_h} K$ be a tetrahedral mesh, and we use lowest-order conforming finite elements

$$V_h = \left\{ \phi_h \in \mathrm{C}^0(\overline{\Omega}) \,:\, \phi_h|_K \in \mathbb{P}_1(K) \text{ for all } K \in \mathcal{K}_h \right\} .$$

We set $\boldsymbol{V}_h = V_h^3$ and $\boldsymbol{V}_{0,h} = \{\boldsymbol{w} \in \boldsymbol{V}_h \,:\, \boldsymbol{w} = \boldsymbol{0} \text{ on } \Gamma_{\mathrm{D}}\}$. The piecewise constants define the discrete space

$$W_h = \{\psi_h \in \mathrm{L}_\infty(\Omega) \,:\, \psi_h|_K \in \mathbb{P}_0(K) \text{ for all } K \in \mathcal{K}_h\} \ ,$$

so that $\nabla\phi \in W_h^3$ for $\phi_h \in V_h$. Let $\Pi_h^0 \,:\, V_h \to W_h$ be the L_2 projection.

For $\Omega_{\mathrm{EP}} \subset \Omega$, we set $\mathcal{K}_{\mathrm{EP},h} = \mathcal{K}_h \cap \Omega_{\mathrm{EP}}$, and we assume $\Omega_{\mathrm{EP}} \cap \Omega_h = \bigcup_{K\in\mathcal{K}_{\mathrm{EP},h}} K$. We set $V_{\mathrm{EP},h} = V_h|_{\overline{\Omega}_{\mathrm{EP}}}$, $W_{\mathrm{EP},h} = W_h|_{\overline{\Omega}_{\mathrm{EP}}}$, and in $\Omega \setminus \Omega_{\mathrm{EP}}$ functions in $V_{\mathrm{EP},h}$ and $W_{\mathrm{EP},h}$ are extended by zero.

For the number of time steps $N \in \mathbb{N}$, we define $\triangle\, t = T/N$. The fully discrete model is determined by the deformation $\boldsymbol{\varphi}_h^n \in \boldsymbol{V}_h$, displacement $\boldsymbol{u}_h^n \in \boldsymbol{V}_{0,h}$, velocity $\boldsymbol{v}_h^n \in \boldsymbol{V}_{0,h}$, acceleration $\boldsymbol{a}_h^n \in \boldsymbol{V}_{0,h}$, deformation gradient $\boldsymbol{F}_h^n = \boldsymbol{I} + \mathrm{D}\boldsymbol{u}_h^n \in W_h^{3\times 3}$, determinant $J_h^n = \det(\boldsymbol{F}_h^n) \in W_h$, stretch $\gamma_{\boldsymbol{f},h}^n \in W_h$, electric potential $v_h^n \in V_{\mathrm{EP},h}$, concentrations $\boldsymbol{c}_h^n \in W_{\mathrm{EP},h}^{d_c}$ and gating variables $\boldsymbol{w}_h^n \in W_{\mathrm{EP},h}^{d_w}$ at $t_n = n \triangle t$ for $n = 0, \dots, N$. We assume that the pressure in the cardiac chambers p_{C}^n, $n = 0, \dots, N$, is given; in a full model this depends on the coupling to the circulatory system.

In time we use a staggered scheme. For the initial deformation and stress from the unloaded reference geometry, we have to solve a static problem for the initial pressure in the cardiac chambers. Then, the dynamic equation for the displacement is approximated by the Newmark β-scheme with parameters β_{N} and γ_{N} resulting in a nonlinear equation in every time step. The ODEs for the gating variables are solved with an exponential update (see [23] for details) locally in every element. For the concentrations, we use the explicit Euler method. Then, the parabolic equation for the electric potential is approximated with the implicit Euler method in time, and finally the ODEs for the stretch are again solved with the explicit Euler method. For simplicity, we use the same time step for all equations in our experiments, since this is sufficient for the evaluation of the mechanical properties. Note that reliable simulations for the electrophysiology require considerably smaller time steps as for the mechanics.

The following algorithm is realized for our numerical experiments:

S0) For $n = 0$ at $t_0 = 0$, compute $\boldsymbol{u}_h^0 \in \boldsymbol{V}_{0,h}$ by solving

$$\int_\Omega \boldsymbol{P}(\boldsymbol{I} + \mathrm{D}\boldsymbol{u}_h^0, \boldsymbol{0}, \boldsymbol{f}) \,:\, \mathrm{D}\boldsymbol{\phi}_h \,\mathrm{d}\boldsymbol{x} = -\int_{\Gamma_{\mathrm{C}}} p_{\mathrm{C}}^0 Cof(\boldsymbol{I} + \mathrm{D}\boldsymbol{u}_h^0)\boldsymbol{n} \cdot \boldsymbol{\phi}_h \,\mathrm{d}\boldsymbol{a} \ , \qquad \boldsymbol{\phi}_h \in \boldsymbol{V}_{0,h} \ .$$

Set the initial values $\boldsymbol{\varphi}_h^0 = id + \boldsymbol{u}_h^0$, $\boldsymbol{v}_h^0 = \boldsymbol{a}_h^0 = \boldsymbol{0}$, $\boldsymbol{F}_h^0 = \boldsymbol{I} + \mathrm{D}\boldsymbol{u}_h^0$, $\boldsymbol{F}_{\mathrm{a},h}^0 = \boldsymbol{I}$, $J_h^0 = \det(\boldsymbol{F}_h^0)$, $\gamma_{\boldsymbol{f},h}^0 = 0$ in Ω for the mechanics, and for the electrophysiology $v_h^0 = v_0$, $c_{h,k}^0 = c_{0,k}$ for $k = 1, \dots, d_{\boldsymbol{c}}$, $w_{h,k}^0 = w_{0,k}$ for $k = 1, \dots, d_{\boldsymbol{w}}$ in Ω_{EP}. Then, set $n = 1$.

S1) Set $\boldsymbol{b}_h^{n-1} = \frac{\rho}{\beta_\mathrm{N}\Delta t^2}\boldsymbol{u}_h^{n-1} + \frac{\rho(1+\alpha_\mathrm{R})}{\beta_\mathrm{N}\Delta t}\boldsymbol{v}_h^{n-1} + \frac{\rho(1-2\beta_\mathrm{N})}{2\beta_\mathrm{N}}\boldsymbol{a}_h^{n-1}$ and compute $\boldsymbol{u}_h^n \in \boldsymbol{V}_{0,h}$ by solving approximately

$$\int_\Omega \left(\frac{\rho}{\beta_\mathrm{N}\Delta t^2}\boldsymbol{u}_h^n \cdot \boldsymbol{\phi}_h + \boldsymbol{P}_\mathrm{eff}\left(\boldsymbol{I} + \mathrm{D}\boldsymbol{u}_h^n, \boldsymbol{v}_h^{n-1}, \boldsymbol{f}, \gamma_{\boldsymbol{f},h}^{n-1}\right) : \mathrm{D}\boldsymbol{\phi}_h \right) \mathrm{d}\boldsymbol{x} = \int_\Omega \boldsymbol{b}_h^{n-1} \cdot \boldsymbol{\phi}_h \, \mathrm{d}\boldsymbol{x} - \int_{\Gamma_\mathrm{C}} p_\mathrm{C}^n Cof(\boldsymbol{I} + \mathrm{D}\boldsymbol{u}_h^0)\boldsymbol{n} \cdot \boldsymbol{\phi}_h \, \mathrm{d}\boldsymbol{a}$$

for all $\boldsymbol{\phi}_h \in \boldsymbol{V}_{0,h}$ with a Newton method. Then, set

$$\boldsymbol{a}_h^n = \frac{1}{\beta_\mathrm{N} \vartriangle t^2}\left(\boldsymbol{u}_h^n - \boldsymbol{u}_h^{n-1}\right) - \frac{1}{\beta_\mathrm{N} \vartriangle t}\boldsymbol{v}_h^{n-1} - \frac{1-2\beta_\mathrm{N}}{2\beta_\mathrm{N}}\boldsymbol{a}_h^n \,, \quad \boldsymbol{v}_h^n = \boldsymbol{v}_h^{n-1} + \vartriangle t\big((1-\gamma_\mathrm{N})\boldsymbol{a}_h^{n-1} + \gamma_\mathrm{N}\boldsymbol{a}_h^n\big) \,, \quad \boldsymbol{u}_h^n = \boldsymbol{u}_h^{n-1} + \vartriangle t\boldsymbol{v}_h^n \,.$$

S2) Compute $\mathbf{w}_h^n \in W_{\mathrm{EP},h}^{d_w}$ by evaluating

$$\boldsymbol{w}_h^n = \boldsymbol{G}_{\boldsymbol{w}}^{\Delta t}\left(\Pi_K(v_h^{n-1}), \boldsymbol{w}_h^{n-1}\right),$$

locally in every element with

$$\boldsymbol{G}_{\boldsymbol{w}}^{\Delta t} = (G_k^{\Delta t}) \,, \quad G_k^{\Delta t}(v, w) = w_{k,\infty}(v) + \big(w - w_{k,\infty}(v)\big)\exp\left(- \vartriangle t\,(\alpha_k(v) + \beta_k(v))\right) \,, \quad w_{k,\infty}(v) = \frac{\alpha_k(v)}{\alpha_k(v) + \beta_k(v)} \,.$$

S3) Compute $\boldsymbol{c}_h^n \in W_{\mathrm{EP},h}^{d_c}$ locally in every element

$$\boldsymbol{c}_h^n = \boldsymbol{c}_h^{n-1} + \vartriangle t\ \mathbf{G}_\mathbf{c}\left(\Pi_K(v_h^{n-1}), \mathbf{w}_h^n, \boldsymbol{c}_h^{n-1}\right) \,.$$

S4) Set $J_h^n = \det \boldsymbol{F}_h^n$ and $\boldsymbol{D}_h^n = \boldsymbol{D}(\boldsymbol{F}_h^n) = J_h^n(\boldsymbol{F}_h^n)^{-1}\boldsymbol{D}_0(\boldsymbol{F}_h^n)^{-\top}$. Compute $v_h^n \in V_{\mathrm{EP},h}$ solving for all $\phi_h \in V_{\mathrm{EP},h}$

$$\int_{\Omega_\mathrm{EP}} (\chi C_\mathrm{m} J_h^n v_h^n \phi_h + \vartriangle t\boldsymbol{D}_h^n \nabla v_h^n \cdot \nabla\phi_h) \, \mathrm{d}\boldsymbol{x} = \int_{\Omega_\mathrm{EP}} \left(\chi C_\mathrm{m} J_h^{n-1} v_h^{n-1} - \vartriangle t J_h^n \chi \left(I_\mathrm{ion}(v_h^{n-1}, \mathbf{w}_h^n, \mathbf{c}_h^n) + I_\mathrm{ext}^n\right)\right) \phi_h \, \mathrm{d}\boldsymbol{x} \,.$$

S5) Compute $\gamma_{\boldsymbol{f},h}^n \in W_{\mathrm{EP},h}$ locally in every element

$$\gamma_{\boldsymbol{f},h}^n = \gamma_{\boldsymbol{f},h}^{n-1} + \vartriangle t G_{\gamma_\mathrm{f}}\left(\gamma_{\boldsymbol{f},h}^{n-1}, \boldsymbol{F}_h^n, \boldsymbol{f}, \boldsymbol{c}_h^n\right) \,.$$

If $n < N$, set $n := n + 1$ and go to S1).

The nonlinear equations in S0) and S1) are solved with a Newton method, where the derivative of the volumetric penalty is computed by the tensor cross product calculus, compare Appendix. Within the Newton iteration the linearization and the linear problem in S4) are solved with a parallel preconditioned GMRES method. For further algorithmic details, we refer to [12, 13, 23].

4 | NUMERICAL EVALUATION OF MECHANICAL MODELS AND PARAMETERS

The simulation study was conducted on a realistic biventricular geometry of a healthy female volunteer derived from magnetic resonance (MR) imaging data. MR images were captured at the University Hospital in Heidelberg. The volunteer gave informed consent and the study was approved by the institutional review board. The finite element mesh was generated using MR images during diastasis, that is, the stage in the heart cycle at which the pressures inside the chambers are lowest (but not zero). To approximate a stress-free reference configuration, we used an iterative approach described in [39] using physiological end-diastolic pressures of 8 mmHg [8] and 4 mmHg [10] for the left and right ventricle, respectively.

In all the subsequent numerical experiments, this biventricular geometry is used as the reference geometry. The corresponding boundary conditions are shown in Figure 1. The atrioventricular valves, marked in orange, are only included

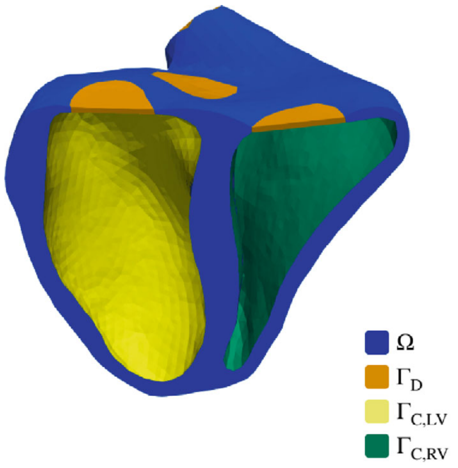

FIGURE 1 Boundary parts Γ_{D} and $\Gamma_{\mathrm{C}} = \Gamma_{\mathrm{C,RV}} \cup \Gamma_{\mathrm{C,LV}}$ for the unloaded geometry Ω.

to enable cavity volume calculations. They are fixated by a homogeneous Dirichlet boundary condition and do not contribute to neither electrophysiology nor elasto-mechanics. An endocardial pressure of 4 and 8 mmHg is applied on the surfaces $\Gamma_{\mathrm{C,RV}}$ marked in green and $\Gamma_{\mathrm{C,LV}}$ marked in yellow.

We use the hyperelastic transversely isotropic Guccione material (2) with material parameters $C_{\mathrm{Gucc}} = 0.29\,\mathrm{kPa}$, $b_{\boldsymbol{f}} = 42$, $b_{\boldsymbol{s}} = 16.8$ and $b_{\boldsymbol{f},\boldsymbol{s}} = 29.4$. These parameters were determined by using a reproduced Klotz-curve fitting algorithm as described in [18, 19].
The numerical simulations are realized in the parallel finite element system M++ [5].

4.1 | Initial deformation of the ventricles

Since every cardiac cycle starts with a prestressed geometry that results from the diastolic blood pressure in the ventricles, our first test studies the inflation of the stress-free reference geometry of the cardiac tissue. This includes a nonlinear boundary condition, since the normal direction of the pressure force depends on the deformation. Therefore, we will solve a purely mechanical and static nonlinear elasticity problem, where the unloaded biventricular geometry will be inflated by applying an endocardial pressure of 8 and 4 mmHg to the left and right ventricles, respectively. To solve this problem, the pressure will be applied incrementally. However, because we are only inflating the stress-free reference geometry, there is no active deformation, therefore $T_{\mathrm{a}} = 0\,\mathrm{kPa}$ for the active stress formulation (6) and $\boldsymbol{F}_{\mathrm{a}} = \boldsymbol{I}$ in the active strain approach (4).

Here, we want to examine how parameter choices for the volumetric penalty that approximates incompressibility affect the volume of the deformed geometry and the ventricular volumes as well as the volume of single elements. Using these distinct volumetric penalties, we are also testing numerical convergence on different mesh resolutions. While other algorithms for determining the load-free configuration as an estimate of the stress-free reference configuration exist, we focus on the effect of the volumetric penalty.

Table 1 shows the convergence behavior for linear conforming elements by investigating the initial and deformed cardiac muscle volume as well as the left and right ventricle volumes at different mesh resolutions. In addition, the range of local volume change, that is, the volume change for single elements, is given for the deformed geometry. For the experiments in this section, we test different volumetric penalties κ_{vol} to show its impact and relevance. The ventricular volumes $|\Omega^{\boldsymbol{\varphi}}_{\mathrm{LV}}|$ and $|\Omega^{\boldsymbol{\varphi}}_{\mathrm{RV}}|$ are computed from the boundary using Gauss's theorem.

Starting with the mesh on level $\ell = 0$, we study the convergence on a sequence of uniformly refined meshes for level $\ell = 1, 2$. We can observe that the initial volume of the geometry is preserved up to 0.1% even for the smallest considered penalty term and the coarsest mesh resolution $\ell = 0$. This can also be seen in Figure 2 where the reference configuration on $\ell = 0$ and the deformed geometries for $\ell = 0, 1, 2$ with corresponding Euclidean norm of the displacement are shown. As expected, the volume is preserved even better if a finer mesh is used and if the violation of incompressibility is penalized more.

TABLE 1 Starting with the initial volume 168 825 mm^3 of the reference geometry, we study the convergence of the cardiac muscle volume $|\Omega^\varphi|$ and the left and right ventricle volumes by uniform refinement and for various volumetric penalties; furthermore, we consider the minimal and maximal local volume changes. DOFs = degrees of freedom.

Level	Elements	DOFs	κ_{vol} (MPa)	$\lvert\Omega^\varphi\rvert$ (mm^3)	Left ventricle (mL)	Right ventricle (mL)	min J	max J
$\ell = 0$	144 656	103 578	1000	168 928	142.524	153.879	0.925	1.097
			2000	168 877	140.191	150.445	0.947	1.071
			10 000	168 836	132.105	140.669	0.968	1.029
$\ell = 1$	1 157 248	703 719	1000	168 926	145.937	159.923	0.905	1.133
			2000	168 875	144.802	157.950	0.923	1.099
			10 000	168 835	140.669	150.548	0.964	1.046
$\ell = 2$	9 257 984	5 129 589	1000	168 925	147.406	162.807	0.797	1.177
			2000	168 875	146.946	161.949	0.859	1.138

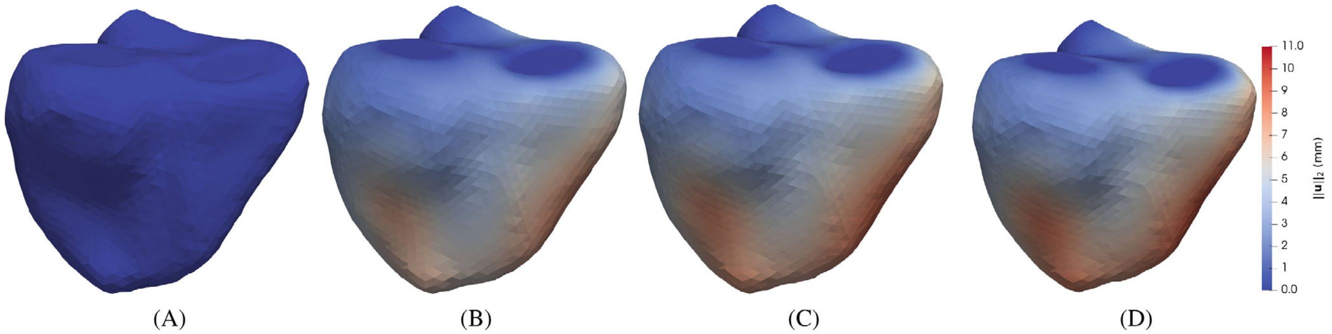

FIGURE 2 Preloading the unloaded reference geometry with $T_a = 0$ kPa for a left ventricle pressure of 8 mmHg and a right ventricle pressure of 4 mmHg with $\kappa_{\text{vol}} = 1$ MPa. (A) Unloaded geometry. (B) Preloaded geometry on $\ell = 0$. (C) Preloaded geometry on $\ell = 1$. (D) Preloaded geometry on $\ell = 2$.

In contrast to the quasi-incompressibility of the global volume, locally in some elements there are a few outliers where the penalty is insufficient. The Jacobian determinant differs substantially from its expected value, namely $J \approx 1$. This becomes even clearer if we take a look at the finer mesh resolutions. The range of the local volume change is increasing, and the deviation gets larger with each level. For example, on $\ell = 0$, there is a deviation up to 8% and on $\ell = 2$ the maximum deviation is about 21%, using $\kappa_{\text{vol}} = 1$ MPa. Even for a markedly greater penalty, namely $\kappa_{\text{vol}} = 10$ MPa, there are still some outliers in the local elements. However, the comparison of the different choices of the volumetric penalty shows that increasing local volume deviation for uniform mesh refinements gets acceptable for larger penalties. This local failure is due to the fact that the volumetric penalty is only performing well for the whole geometry volume and not for every single element.

Investigating the results with regard to the various penalty choices, we can observe that the differences in the volume changes of the ventricles between smallest and largest chosen penalty is greater than the difference between the uniform mesh resolutions under fixed penalty. For example, comparing $\kappa_{\text{vol}} = 1$ MPa and $\kappa_{\text{vol}} = 10$ MPa on $\ell = 0$, there is a variation in the ventricle volumes of approximately 8%.

The variation of using diverse penalty terms can also be seen in Figure 3, where the deformation of endocardial and epicardial surfaces under the use of different penalties is shown. In contrast, we can observe linear convergence in Table 1 for fixed volumetric penalty and uniform mesh refinement, which is expected due to the use of linear conforming elements. However, the large distinction between using different penalty terms, gets less for finer meshes. Hence, the distinction could be due to the fact of only using and comparing lowest-order conforming elements. Therefore, the choice of the penalty term is crucial for these kinds of finite elements. We also expect that using higher-order conforming elements or more stabilized finite elements could improve this behavior. Furthermore, instead of employing W_{vol} in (3), it is feasible to examine the impact of investigating diverse volumetric penalty functions.

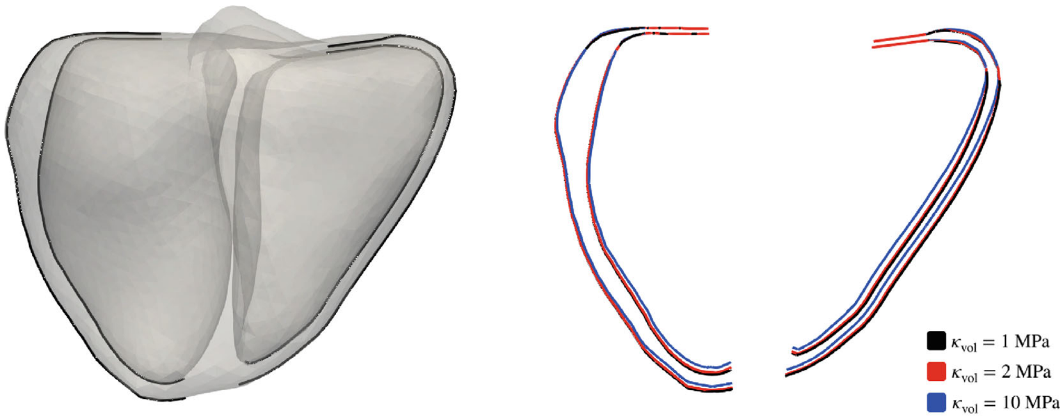

(A) (B)

FIGURE 3 Location of the endocardial and epicardial walls of the ventricles in the preloaded geometry on $\ell = 0$ (left) and comparison of the deformed walls using different volumetric penalties on $\ell = 0$ (right). (A) Lines of interest in the preloaded geometry. (B) Deformed lines of interest in the preloaded geometry, using different volumetric penalties.

4.2 | Contraction by active strain and active stress—a comparison

In this section, we extend the purely mechanic and static benchmark setting of problem 3, introduced in [21], which deals with the inflation and active contraction of an idealized ventricle, in two ways. On the one hand, we use a more complex and anatomically more realistic biventricular geometry. The geometry and the sheet and normal directions for this test are taken from [14]. We apply an endocardial pressure of 8 and 4 mmHg in the left and right ventricle, respectively. Moreover, we penalize the violation of incompressibility by $\kappa_{\mathrm{vol}} = 1$ MPa. On the other hand, we want to set up a comparison between the active stress approach, used in [21], and the active strain approach to cause contraction. The active stress is given by a constant second Piola-Kirchhoff stress in fiber direction (6). For this benchmark configuration, we select $T_{\mathrm{a}} = 35\,\mathrm{kPa}$. This is compared with the active strain using the more general ansatz [33, Sect. 6.2.1], [36] with a scaling factor $s_\gamma \approx 1$

$$\boldsymbol{F}_{\mathrm{a}} = \begin{cases} (1+\gamma_{\boldsymbol{f}})\boldsymbol{f}\boldsymbol{f}^\top + \frac{1}{s_\gamma\sqrt{1+\gamma_{\boldsymbol{f}}}}\boldsymbol{s}\boldsymbol{s}^\top + \frac{s_\gamma}{\sqrt{1+\gamma_{\boldsymbol{f}}}}\boldsymbol{t}\boldsymbol{t}^\top, & \text{if } 1+\gamma_{\boldsymbol{f}} > 0, \\ \boldsymbol{I}, & \text{else,} \end{cases} \tag{8}$$

depending on the fiber $\boldsymbol{f}$, sheet $\boldsymbol{s}$, and sheet-normal $\boldsymbol{t}$. Since $\boldsymbol{f}\boldsymbol{f}^\top + \boldsymbol{s}\boldsymbol{s}^\top + \boldsymbol{t}\boldsymbol{t}^\top = \boldsymbol{I}$, (8) is identical to (5) for $s_\gamma = 1$.

However, (8), has more free parameters and therefore more possibilities to adapt the active strain model to the active stress formulation. To achieve a similar setting as that of the active stress formulation, the cellular stretch $\gamma_{\boldsymbol{f}}$ is chosen as constant. With parameter studies and fitting for the free parameters in the active strain formulation, namely the stretch and the scaling factor s_γ, we aimed to achieve comparable results to those with active stress. We obtained the closest match for $\gamma_{\boldsymbol{f}} = 0.8$ and $s_\gamma = 0.9, 1.0$. Note that we increment the pressure iteratively and add simultaneously the whole active stress or active strain at once to solve the quasi-static nonlinear elasticity problem.

Starting from the initial volume $168\,825\,\mathrm{mm}^3$ of the reference geometry, we study the convergence by uniform refinement for the different approaches. Tables 2–4 show that both approaches are converging and lead to meaningful results. Furthermore, we can observe again the globally well-preserved cardiac muscle volume, although the active strain approach is preserving the volume slightly better, especially for the choice $\gamma_{\boldsymbol{f}} = 0.8$ and $s_\gamma = 0.9$. This aspect can also be considered for the local outliers. For instance, for the finest mesh resolution, the local volume change is approximately 70%, whereas the active strain exhibits a deviation of 37%. When comparing the two different active strain variants, it is noticeable that the ventricular volumes get larger when the scaling factor is increased. However, despite many parameter studies to approximate the active stress with the free parameters of the active strain, it was not possible to achieve identical results in this setting. Figure 4 shows the endocardial and epicardial deformed walls

TABLE 2 Active stress, $T_\mathrm{a} = 35\,\mathrm{kPa}$.

Level	Elements	DOFs	$\lvert\Omega^\varphi\rvert$ (mm^3)	Volume left ventricle (mL)	Volume right ventricle (mL)	min J	max J
0	144 656	103 578	167 402	77.239	83.695	0.791	1.159
1	1 157 248	703 719	167 431	76.499	91.524	0.667	1.206
2	9 257 984	5 129 589	167 448	76.485	93.323	0.306	1.478

TABLE 3 Active strain, $\gamma_f = 0.8$ and $s_\gamma = 0.9$.

Level	Elements	DOFs	$\lvert\Omega^\varphi\rvert$ (mm^3)	Volume left ventricle (mL)	Volume right ventricle (mL)	min J	max J
0	144 656	103 578	168 494	78.634	90.535	0.819	1.107
1	1 157 248	703 719	168 645	77.261	100.793	0.747	1.139
2	9 257 984	5 129 589	168 721	77.047	105.486	0.632	1.246

TABLE 4 Active strain, $\gamma_f = 0.8$ and $s_\gamma = 1.0$.

Level	Elements	DOFs	$\lvert\Omega^\varphi\rvert$ (mm^3)	Volume left ventricle (mL)	Volume right ventricle (mL)	min J	max J
0	144 656	103 578	168 286	82.396	92.585	0.824	1.096
1	1 157 248	703 719	168 446	81.584	102.761	0.729	1.146
2	9 257 984	5 129 589	168 530	81.622	107.149	0.648	1.192

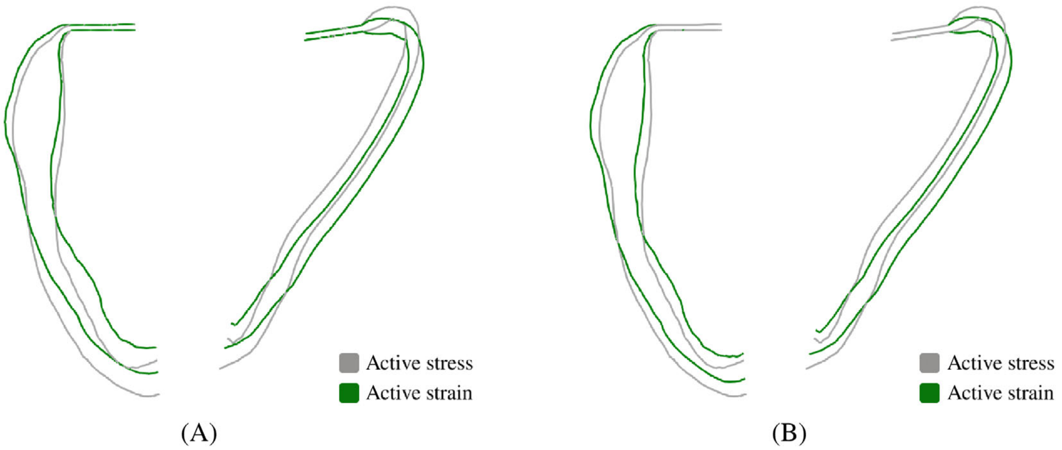

(A)

(B)

FIGURE 4 Comparison of deformed endocardial and epicardial ventricular walls using the active stress approach with $T_\mathrm{a} = 35\,\mathrm{kPa}$ and the active strain approach with stretch $\gamma_f = 0.8$ and different scaling factors s_γ on $\ell = 1$. (A) $s_\gamma = 0.9$; (B) $s_\gamma = 1.0$.

of the ventricles under the use of the active stress approach (gray) and the best choices for the active strain approach (green). We can see that there are differences in several aspects, especially the ventricular volumes are larger for the active strain approach. This becomes even clearer in Figure 5 where the active stress is compared with the active strain approach generated with $\gamma_f = 0.8$ and scaling factor $s_\gamma = 1.0$ from different views. The deformed geometry under the use of the active stress formulation is slightly more pointed, the geometry appears more stretched in long axis, whereas the deformed geometry generated using the active strain approach is more stretched in width. It is necessary to find a good compromise between similar blood volumes or shapes. Nevertheless, one could also use a different formula for $\boldsymbol{F}_\mathrm{a}$ than (8) or use more stabilized or higher-order elements to enhance the results and eventually attain more similar outcomes.

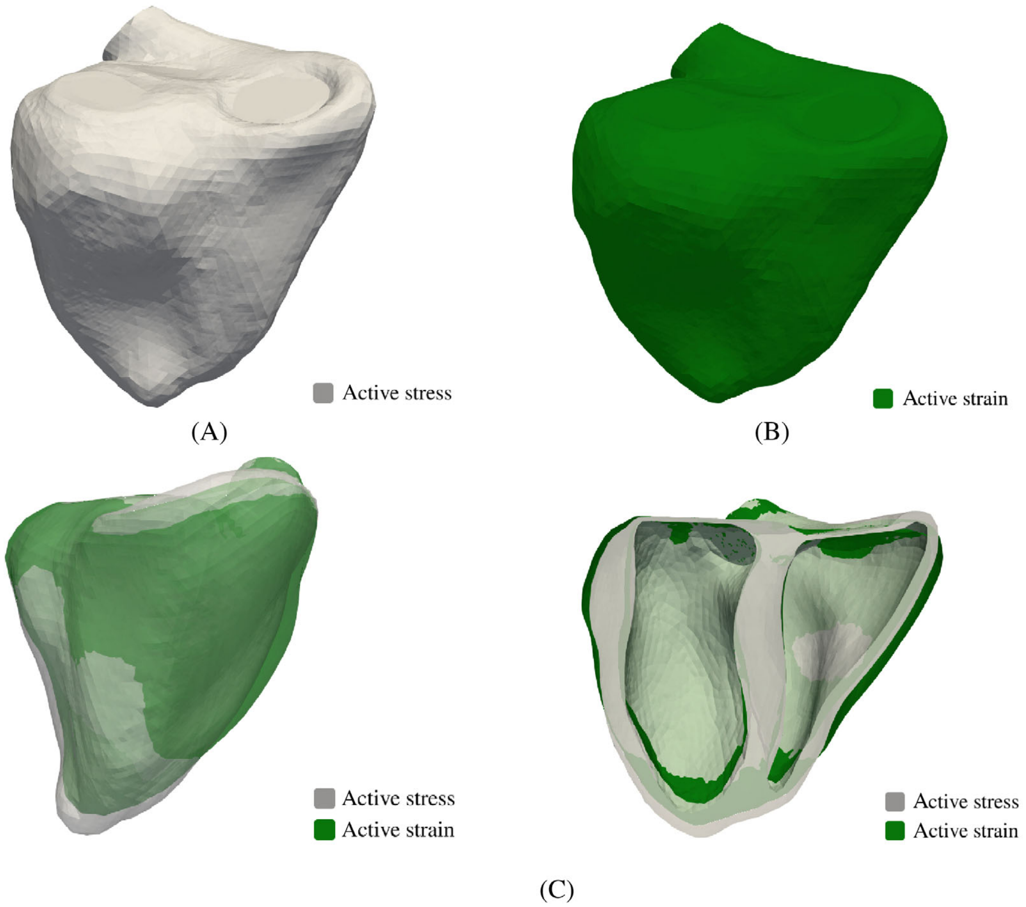

FIGURE 5 Preloading unloaded geometry under the use of the active stress approach with active tension $T_\mathrm{a} = 35$ kPa and the active strain approach with $\gamma_{\boldsymbol{f}} = 0.8$ and $s_\gamma = 1.0$ on $\ell = 1$. (A) Active stress approach with $T_a = 35$ kPa. (B) Active strain approach with $\gamma_{\boldsymbol{f}} = 0.8$ and $s_\gamma = 1.0$. (C) Comparison of active strain and active stress approach from different perspectives.

4.3 | Comparison of numerical damping with a viscous model

We will examine the coupled PDE-ODE system described in (1). To initiate the system, the unloaded geometry is preloaded precisely as detailed in Section 4.1. The cardiac cycle is then simulated utilizing the staggered numerical approximation scheme outlined in Section 3 and specified for the electrophysiology in [23]. We choose the length of a typical heartbeat (0.8 s) as time interval. For the electrophysiology, we use the ten Tusscher et al. cell model [41] with the same parameters as in Niederer et al. [27] and the activation pattern in [23]. The corresponding evolution of the electric potential is illustrated in Figure 6.

The ten Tusscher et al. cell model is supplemented by the stretch model in (7). Due to the utilization of the transversely isotropic Guccione material, we use, in contrast to [37], $\mu_{\boldsymbol{f}} = 1000$ s $\mu\mathrm{M}^{-2}$ and $\alpha_{\boldsymbol{f}} = -10$ $\mu\mathrm{M}^{-2}$ in (7), as obtained from parameter studies. The remaining parameters in the tension update, namely $c_0^{\mathrm{FL}}, \dots, c_3^{\mathrm{FL}}, d_1^{\mathrm{FL}}, \dots, d_3^{\mathrm{FL}}, \ell_{\mathrm{R,min}}, \ell_{\mathrm{R,max}}, \ell_{\mathrm{R,0}}$, are chosen as in Rossi et al. [37]. The calcium concentration c_{Ca} is dynamically determined by the ten Tusscher et al. cell model. The obtained update for $\gamma_{\boldsymbol{f}}$ is used to adjust the stretch required for the active strain approach (5), which is solely taken into account in this instance. To achieve quasi-incompressibility, we use a penalty of 1 MPa, and chose the mass density $\rho = 1028$ kg m^{-3} in (1d) for the dynamic nonlinear elasticity equations.

To reduce numerical oscillations occurring in explicit time integration schemes [6], we compare two damping models for cardiac elastodynamics. The first method, known as the Newmark β-scheme [17], employs a numerical time-stepping that incorporates an inherent damping effect, while the second method, the Rayleigh damping [20, 38], is a physical damping. The Newmark scheme is unconditionally stable for $\beta_{\mathrm{N}} \geq 0.5, \gamma_{\mathrm{N}} \geq 0.25$ and for $\gamma_{\mathrm{N}} > 0.5$ it provides a numerical damping effect [6, Sect. 6.3.3]. Therefore, for the damped Newmark scheme without viscosity ($\alpha_{\mathrm{R}} = 0$ s^{-1}), we are using $\beta_{\mathrm{N}} = 0.3$ and $\gamma_{\mathrm{N}} = 0.6$. For the Rayleigh damping, we use $\beta_{\mathrm{N}} = 0.25$, $\gamma_{\mathrm{N}} = 0.5$, and $\alpha_{\mathrm{R}} = 200$ s^{-1}. This selection was based

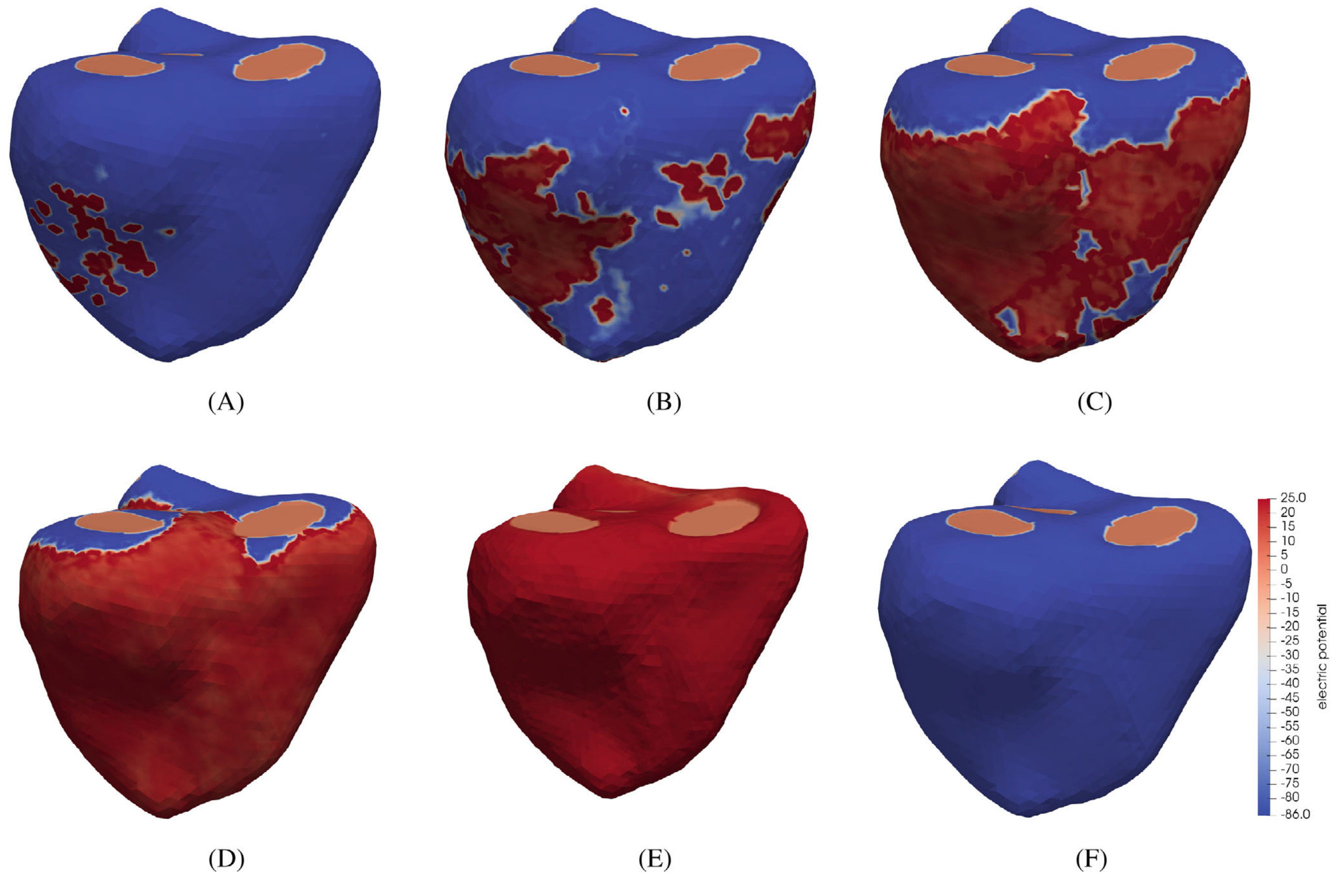

FIGURE 6 Evolution of the electric potential v_m (in mV) during the cardiac cycle. (A) $t = 20$ ms. (B) $t = 30$ ms. (C) $t = 40$ ms. (D) $t = 60$ ms. (E) $t = 110$ ms. (F) $t = 500$ ms.

TABLE 5 Convergence in space and time for Newmark method with numerical damping.

Level	Elements	DOFs	$\triangle t$ (ms)	$\lvert\Omega^{\varphi}\rvert$ (mm^3)	Volume left ventricle (mL)	Volume right ventricle (mL)
0	144 656	103 578	1	168 927	141.764	153.224
			0.5	168 922	141.635	147.678
			0.25	168 919	141.578	145.796
1	1 157 248	703 719	1	168 912	143.911	156.894
			0.5	168 905	142.947	155.888
			0.25	168 912	143.983	157.589
2	9 257 984	5 129 589	1	168 921	145.995	161.619

on parameter studies and resulted in good damping properties. In addition, we test the convergence in time for a fixed mesh resolution in space and the convergence in space with a fixed time step $\triangle t$.

In Tables 5 and 6, we examine the convergence for the cardiac muscle volume and the ventricle volumes at the end of the cardiac cycle utilizing the damped Newmark method and the Rayleigh damping for $\ell = 0, 1, 2$. For $\triangle t = 1$ ms, we observe that all volumes, especially the left and right ventricular volumes at the end of the cycle, that is, at time $t = 800$ ms, are remarkably alike and differ only slightly. The differences can be explained by the occurrence of several oscillations that arise with the use of the damped Newmark procedure. This is also demonstrated in Figure 7, where we plotted the deformed volumes of the left and right ventricles throughout the whole cardiac cycle on $\ell = 1$.

TABLE 6 Convergence in space using the Rayleigh damping with fixed time step of $\triangle t = 1$ ms.

Level	Elements	DOFs	$\|\Omega^{\varphi}\|$ (mm^3)	Volume left ventricle (mL)	Volume right ventricle (mL)
0	144 656	103 578	168 928	142.522	153.852
1	1 157 248	703 719	168 926	145.940	159.900
2	9 257 984	5 129 589	168 925	147.414	162.762

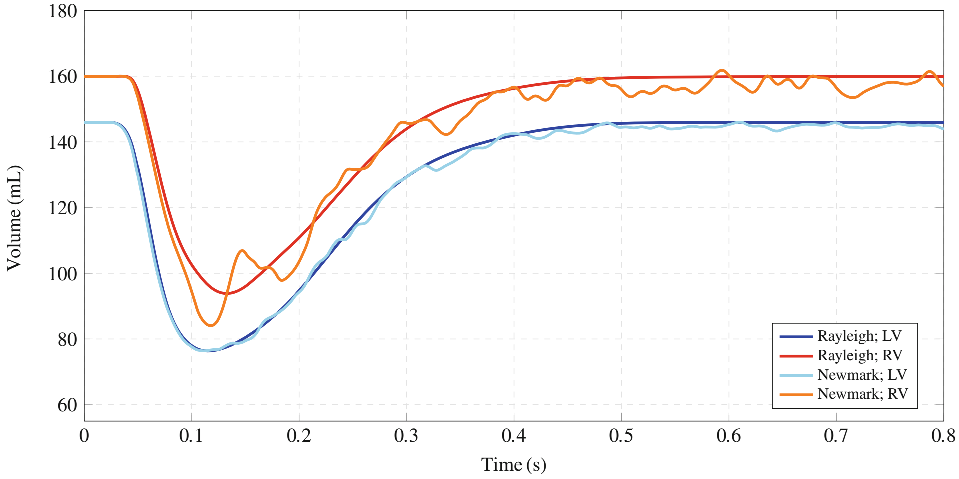

FIGURE 7 Comparison of the Newmark method and the Rayleigh damping for a whole cardiac cycle using $\triangle t = 1$ ms on $\ell = 1$.

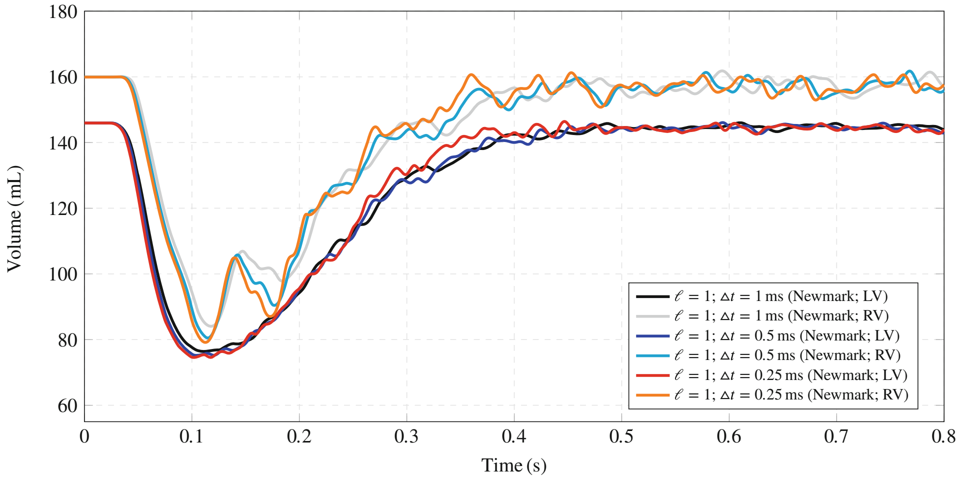

FIGURE 8 Comparison of damped Newmark method for a whole cardiac cycle on $\ell = 1$, using different mechanical time steps and a fixed time step for electrophysiology of 1 ms.

It should be noted that Newmark's oscillations decrease when using finer meshes or higher-order elements. However, the use of Rayleigh damping yields smooth volume curves over time without any oscillations, even when using lowest-order elements. Therefore, the chosen damping parameters render the numerical Newmark damping insufficient, even though the oscillations are less noticeable for the left ventricle volume curve. Tables 5, 6 and Figure 7 illustrate that the ventricle volumes are almost the same as those obtained after preloading the unloaded geometry, as shown in Table 1. In addition, this aspect confirms the validity of our code and demonstrates convergence for both damping methods. In Figure 8, no convergence in time for the Newmark method can be observed.

In summary, physical damping alone is adequate and there is no requirement for supplementary numerical damping. Nevertheless, there are several options for physical damping; alternatively, one may use a Kelvin-Voigt model or only boundary damping on the pericardium, as we used with a mortar coupling in [11].

Here we use the active strain model. For the active stress model the tests with and without Rayleigh damping in [13, App. A] also confirm that viscosity is required to avoid oscillations.

5 | CONCLUSIONS

In this paper, we discussed the mechanical properties of purely mechanical and coupled electro-mechanical models. For all experiments, we used a realistc biventricular geometry. In a static mechanical setting, our numerical experiments demonstrated that the choice of the volumetric penalty to achieve incompressibility is crucial. Globally, using lowest-order conforming finite elements, we could observe linear convergence for the chamber volumes. In contrast, single elements showed outliers in analogy to the locking effect of lowest-order approximations with high volumetric penalties. The considered volumetric penalty is insufficient for these kind of elements. In an extended benchmark setting for the inflation and contraction of the heart, we tested the active stress and active strain formulations. We can conclude that there are several differences between the active stress and active strain approaches. With the used update formula for the active deformation in the active strain model, it was not possible to obtain identical outcomes to those from active stress. Performing a full cardiac cycle in the coupled electro-mechanical setting, we compared numerical damping with a visco-elastic model. We observed that the Newmark damping is not sufficient; physical damping, like Rayleigh damping, is necessary.

To improve the conservation of the local volume change and to avoid locking effects, in the next step we want to test higher-order conforming elements as well as more stabilized finite elements, for example, discontinuous Galerkin and enriched Galerkin elements. In addition, we will investigate the effect of using different volumetric penalty functions. Using improved finite element discretizations, we expect to achieve improved local incompressibility. We also plan to investigate different update formulas for the active deformation $\boldsymbol{F}_{\mathrm{a}}$ in the active strain model and to extend the comparison with active stress to the dynamics. Furthermore, considering the coupled electro-mechanical model, we will compare boundary damping in combination with coupling to the circulatory system to damping in the cardiac tissue by visco-elasticity using Rayleigh or Kelvin-Voigt models.

AUTHOR CONTRIBUTIONS

Jonathan Fröhlich: Software, data curation, writing. **Tobias Gerach**: Software, data curation. **Jonathan Krauß**: Software, writing – reviewing and editing, investigation. **Axel Loewe**: Conceptualization, reviewing and editing, supervision. **Laura Stengel**: Software, data curation, writing – original draft preparation, writing- reviewing and editing, visualization, investigation. **Christian Wieners**: Software, conceptualization, writing – original draft preparation, writing – reviewing and editing, supervision.

ACKNOWLEDGEMENTS

This article is funded by the Deutsche Forschungsgemeinschaft (DFG, German Research Foundation)—Project-ID 465189069 within the SPP 2311 and Project-ID 258734477 (CRC 1173).

CONFLICT OF INTEREST STATEMENT

The authors declare no potential conflict of interests.

ORCID

Tobias Gerach https://orcid.org/0000-0002-5101-2840
Jonathan Krauß https://orcid.org/0000-0001-8823-3906
Axel Loewe https://orcid.org/0000-0002-2487-4744
Christian Wieners https://orcid.org/0000-0001-6242-6777

REFERENCES

[1] D. Ambrosi and S. Pezzuto, Active stress vs. active strain in mechanobiology: constitutive issues, J. Elast. **107** (2012), 199–212.
[2] D. Ambrosi, G. Arioli, F. Nobile, and A. Quarteroni, Electromechanical coupling in cardiac dynamics: the active strain approach, SIAM J. Appl. Math. **71** (2011), no. 2, 605–621.

[3] R. Andlauer, G. Seemann, L. Baron, O. Dössel, P. Kohl, P. Platonov, and A. Loewe, Influence of left atrial size on P-wave morphology: differential effects of dilation and hypertrophy, Europace **20** (2018), no. S3, iii36–iii44. https://doi.org/10.1093/europace/euy231

[4] H. J. Arevalo, F. Vadakkumpadan, E. Guallar, A. Jebb, P. Malamas, K. C. Wu, and N. A. Trayanova, Arrhythmia risk stratification of patients after myocardial infarction using personalized heart models, Nat. Commun. **7** (2016), 11437.

[5] N. Baumgarten and C. Wieners, The parallel finite element system m++ with integrated multilevel preconditioning and multilevel Monte Carlo methods, Comput. Math. Appl. **81** (2021), 391–406. Development and Application of Open-source Software for Problems with Numerical PDEs.

[6] T. Belytschko, W. K. Liu, and B. Moran, *Nonlinear finite elements for continua and structures*, Wiley, Chichester, 2000.

[7] J. Bonet, A. J. Gil, and R. Ortigosa, A computational framework for polyconvex large strain elasticity, Comput. Methods Appl. Mech. Eng. **283** (2015), 1061–1094.

[8] E. Braunwald, E. C. Brockenbrough, C. J. Frahm, and J. Ross Jr., Left atrial and left ventricular pressures in subjects without cardiovascular disease: observations in eighteen patients studied by transseptal left heart catheterization, Circulation **24** (1961), no. 2, 267–269.

[9] M. Fedele, R. Piersanti, F. Regazzoni, M. Salvador, P. C. Africa, M. Bucelli, A. Zingaro, L. Dede', and A. Quarteroni, A comprehensive and biophysically detailed computational model of the whole human heart electromechanics, Comput. Methods Appl. Mech. Eng. **410** (2023), 115983.

[10] N. O. Fowler, R. N. Westcott, and R. C. Scott, Normal pressure in the right heart and pulmonary artery, Am. Heart J. **46** (1953), no. 2, 264–267. https://www.sciencedirect.com/science/article/pii/0002870353902051.

[11] T. Fritz, C. Wieners, G. Seemann, H. Steen, and O. Dössel, Simulation of the contraction of the ventricles in a human heart model including atria and pericardium, Biomech. Model. Mechanobiol. **13** (2013), 627–641.

[12] J. S. Fröhlich. *A segregated finite element method for cardiac elastodynamics in a fully coupled human heart model*, Ph.D. thesis, Karlsruher Institut für Technologie (KIT). 2022 https://doi.org/10.5445/IR/1000150230.

[13] T. Gerach. *Personalized electromechanical modeling of the human heart. Challenges and opportunities for the simulation of pathophysiological scenarios*, Ph.D. thesis, Karlsruher Institut für Technologie (KIT). 2022 https://doi.org/10.5445/IR/1000147806.

[14] T. Gerach, S. Schuler, J. Fröhlich, L. Lindner, E. Kovacheva, R. Moss, E. M. Wülfers, G. Seemann, C. Wieners, and A. Loewe, Electro-mechanical whole-heart digital twins: a fully coupled multi-physics approach, Mathematics **9** (2021), 11. https://doi.org/10.3390/math9111247.

[15] G. Giantesio, A. Musesti, and D. Riccobelli, A comparison between active strain and active stress in transversely isotropic hyperelastic materials, J. Elast. **137** (2019), no. 1, 63–82.

[16] J. M. Guccione, K. D. Costa, and A. D. McCulloch, Finite element stress analysis of left ventricular mechanics in the beating dog heart, J. Biomech. **28** (1995), no. 10, 1167–1177. https://www.sciencedirect.com/science/article/pii/0021929094001743.

[17] T. J. Hughes, K. S. Pister, and R. L. Taylor, Implicit-explicit finite elements in nonlinear transient analysis, Comput. Methods Appl. Mech. Eng. **17-18** (1979), 159–182. https://www.sciencedirect.com/science/article/pii/0045782579900860.

[18] E. Kovacheva. *Model based estimation of the elastomechanical properties of the human heart*, Ph.D. thesis, Karlsruher Institut für Technologie (KIT). 2021 https://doi.org/10.5445/IR/1000135416.

[19] E. Kovacheva, L. Baron, S. Schuler, T. Gerach, O. Dössel, and A. Loewe, Optimization framework to identify constitutive law parameters of the human heart, Curr. Direct. Biomed. Eng. **6** (2020), no. 3, 95–98. https://doi.org/10.1515/cdbme-2020-3025.

[20] P. Lafortune, R. Arís, M. Vázquez, and G. Houzeaux, Coupled electromechanical model of the heart: parallel finite element formulation, Int. J. Numer. Methods Biomed. Eng. **28** (2012), no. 1, 72–86.

[21] S. Land, V. Gurev, S. Arens, C. M. Augustin, L. Baron, R. Blake, C. Bradley, S. Castro, A. Crozier, M. Favino, T. E. Fastl, T. Fritz, H. Gao, A. Gizzi, B. E. Griffith, D. E. Hurtado, R. Krause, X. Luo, M. P. Nash, S. Pezzuto, G. Plank, S. Rossi, D. Ruprecht, G. Seemann, N. P. Smith, J. Sundnes, J. J. Rice, N. Trayanova, D. Wang, Z. J. Wang, and S. A. Niederer, Verification of cardiac mechanics software: benchmark problems and solutions for testing active and passive material behaviour, Proc. R. Soc. Lond. A **471** (2015), no. 2184, 2015.0641.

[22] H. Lehrmann, A. S. Jadidi, J. Minners, J. Chen, B. Müller-Edenborn, R. Weber, O. Dössel, T. Arentz, and A. Loewe, Novel electrocardiographic criteria for real-time assessment of anterior mitral line block, JACC Clin. Electrophysiol. **4** (2018), no. 7, 920–932. https://doi.org/10.1016/j.jacep.2018.03.007

[23] L. P. Lindner, T. Gerach, T. Jahnke, A. Loewe, D. Weiss, and C. Wieners, Efficient time splitting schemes for the monodomain equation in cardiac electrophysiology, Int. J. Numer. Method. Biomed. Eng. **39** (2022), e3666. https://doi.org/10.1002/cnm.3666.

[24] A. Loewe, E. Poremba, T. Oesterlein, A. Luik, C. Schmitt, G. Seemann, and O. Dössel, Patient-specific identification of atrial flutter vulnerability - a computational approach to reveal latent reentry paths, Front. Phys. **9** (2019), 1910. https://doi.org/10.3389/fphys.2018.01910

[25] J. Lumens and T. Delhaas, Cardiovascular modeling in pulmonary arterial hypertension: Focus on mechanisms and treatment of right heart failure using the circadapt model, Am. J. Cardiol. **110** (2012), no. 6, Supplement, S39–S48. https://www.sciencedirect.com/science/article/pii/S0002914912015469, the Right Ventricle in Pulmonary Arterial Hypertension.

[26] S. A. Niederer, J. Lumens, and N. A. Trayanova, Computational models in cardiology, Nat. Rev. Cardiol. **26** (2019). 100–111.

[27] S. A. Niederer, E. Kerfoot, A. P. Benson, M. O. Bernabeu, O. Bernus, C. Bradley, E. M. Cherry, R. Clayton, F. H. Fenton, A. Garny, E. Heidenreich, S. Land, M. Maleckar, P. Pathmanathan, G. Plank, J. F. Rodríguez, I. Roy, F. B. Sachse, G. Seemann, O. Skavhaug, and N. P. Smith, Verification of cardiac tissue electrophysiology simulators using an N-version benchmark, Phil. Trans. R. Soc. A **369** (2011), no. 1954, 4331–4351.

[28] F. Nobile, A. Quarteroni, and R. Ruiz-Baier, An active strain electromechanical model for cardiac tissue, Int. J. Numer. Methods Biomed. Eng. **28** (2012), no. 1, 52–71.

[29] D. Ogiermann, D. Balzani, and L. E. Perotti, "*An extended generalized Hill model for cardiac tissue: Comparison with different approaches based on experimental data*," *International conference on functional imaging and modeling of the heart*, O. Bernard, P. Clarysse, N. Duchateau, J. Ohayon, and M. Viallon (eds.), Springer, Cham, 2023, pp. 555–564.

[30] M. Peirlinck, F. S. Costabal, J. Yao, J. Guccione, S. Tripathy, Y. Wang, D. Ozturk, P. Segars, T. Morrison, S. Levine, and E. Kuhl, Precision medicine in human heart modeling: perspectives, challenges, and opportunities, Biomech. Model. Mechanobiol. **20** (2021), 803–831.

[31] M. R. Pfaller, J. M. Hörmann, M. Weigl, A. Nagler, R. Chabiniok, C. Bertoglio, and W. A. Wall, The importance of the pericardium for cardiac biomechanics: from physiology to computational modeling, Biomech. Model. Mechanobiol. **18** (2019), no. 2, 503–529.

[32] A. Prakosa, H. J. Arevalo, D. Deng, P. M. Boyle, P. P. Nikolov, H. Ashikaga, J. J. E. Blauer, E. Ghafoori, C. J. Park, R. C. Blake III, F. T. Han, R. S. MacLeod, H. R. Halperin, D. J. Callans, R. Ranjan, J. Chrispin, S. Nazarian, and N. A. Trayanova, Personalized virtual-heart technology for guiding the ablation of infarct-related ventricular tachycardia, Nat. Biomed. Eng. **2** (2018), 732–740.

[33] A. Quarteroni, L. Dedè, A. Manzoni, and C. Vergara, *Mathematical modelling of the human cardiovascular system: data, numerical approximation, clinical applications*, Vol **33**, Cambridge University Press, Cambridge, 2019.

[34] F. Regazzoni and A. Quarteroni, Accelerating the convergence to a limit cycle in 3D cardiac electromechanical simulations through a data-driven 0D emulator, Comput. Biol. Med. **135** (2021), 104641.

[35] F. Regazzoni, M. Salvador, P. C. Africa, M. Fedele, L. Dedè, and A. Quarteroni, A cardiac electromechanical model coupled with a lumped-parameter model for closed-loop blood circulation, J. Comput. Phys. **457** (2022), 111083.

[36] S. Rossi, R. Ruiz-Baier, L. F. Pavarino, and A. Quarteroni, Orthotropic active strain models for the numerical simulation of cardiac biomechanics, Int. J. Numer. Methods Biomed. Eng. **28** (2012), no. 6-7, 761–788.

[37] S. Rossi, T. Lassila, R. Ruiz-Baier, A. Sequeira, and A. Quarteroni, Thermodynamically consistent orthotropic activation model capturing ventricular systolic wall thickening in cardiac electromechanics, Eur. J. Mech. A Solids **48** (2014), 129–142 Frontiers in Finite-Deformation Electromechanics.

[38] A. Santiago, J. Aguado-Sierra, M. Zavala-Aké, R. Doste-Beltran, S. Gómez, R. Arís, J. C. Cajas, E. Casoni, and M. Vázquez, Fully coupled fluid-electro-mechanical model of the human heart for supercomputers, Int. J. Numer. Methods Biomed. Eng. **34** (2018), no. 12, e3140. https://doi.org/10.1002/cnm.3140.

[39] M. Sellier, An iterative method for the inverse elasto-static problem, J. Fluids Struct. **27** (2011), no. 8, 1461–1470 https://www.sciencedirect.com/science/article/pii/S088997461100123X.

[40] M. Strocchi, M. A. Gsell, C. M. Augustin, O. Razeghi, C. H. Roney, A. J. Prassl, E. J. Vigmond, J. M. Behar, J. S. Gould, C. A. Rinaldi, M. J. Bishop, G. Plank, and S. A. Niederer, Simulating ventricular systolic motion in a four-chamber heart model with spatially varying Robin boundary conditions to model the effect of the pericardium, J. Biomech. **101** (2020), 109645. https://doi.org/10.1016/j.jbiomech.2020.109645.

[41] K. H. W. J. ten Tusscher and A. V. Panfilov, Alternans and spiral breakup in a human ventricular tissue model, Amer. J. Physiol. Heart Circul. Physiol. **291** (2006), no. 3, H1088–H1100.

How to cite this article: J. Fröhlich, T. Gerach, J. Krauß, A. Loewe, L. Stengel, and C. Wieners, *Numerical evaluation of elasto-mechanical and visco-elastic electro-mechanical models of the human heart*, GAMM-Mitteilungen. **46** (2023), e202370010. https://doi.org/10.1002/gamm.202370010

APPENDIX. THE TENSOR CROSS PRODUCT

To evaluate the derivatives of $\det(\mathrm{D}\boldsymbol{u})$ and $\mathit{Cof}(\mathrm{D}\boldsymbol{u})$ we use the calculus in [7, Appendix] extending the vector product to tensors. For matrices $\boldsymbol{A}, \boldsymbol{B} \in \mathbb{R}^{3\times 3}$ and vectors $\boldsymbol{v}, \boldsymbol{w} \in \mathbb{R}^3$, the matrices $\boldsymbol{v} \times \boldsymbol{A}, \boldsymbol{B} \times \boldsymbol{w}, \boldsymbol{A} \times \boldsymbol{B} \in \mathbb{R}^{3\times 3}$ are defined by

$$(\boldsymbol{v} \times \boldsymbol{A})\boldsymbol{w} = \boldsymbol{v} \times (\boldsymbol{A}\boldsymbol{w}) \,, \qquad (\boldsymbol{B} \times \boldsymbol{w})\boldsymbol{v} = \boldsymbol{B}(\boldsymbol{w} \times \boldsymbol{v}) \,, \qquad \boldsymbol{v} \cdot (\boldsymbol{A} \times \boldsymbol{B})\boldsymbol{w} = (\boldsymbol{v} \times \boldsymbol{A}) : (\boldsymbol{B} \times \boldsymbol{w}).$$

This implies $\boldsymbol{v} \times \boldsymbol{A} = -\boldsymbol{A}^\top \times \boldsymbol{v}$, $\boldsymbol{A} \times \boldsymbol{B} = \boldsymbol{B} \times \boldsymbol{A}$, and $(\boldsymbol{A} \times \boldsymbol{B}) : \boldsymbol{C} = (\boldsymbol{B} \times \boldsymbol{C}) : \boldsymbol{A} = (\boldsymbol{A} \times \boldsymbol{C}) : \boldsymbol{B}$.

In particular, we have $\mathit{Cof}\,\boldsymbol{A} = \frac{1}{2}\boldsymbol{A} \times \boldsymbol{A}$ and $\det \boldsymbol{A} = \frac{1}{6}\boldsymbol{A} : (\boldsymbol{A} \times \boldsymbol{A})$. From this we also get the identity $\mathit{Cof}\,\boldsymbol{A} = (\det \boldsymbol{A})\boldsymbol{A}^{-\top}$.

For the volumetric penalty we get $W_{\mathrm{vol}}(J) = \frac{1}{2}\left(\frac{1}{6}\boldsymbol{F} : (\boldsymbol{F} \times \boldsymbol{F}) - 1\right)^2$ and thus

$$\begin{aligned} \mathrm{D}_{\boldsymbol{F}} W_{\mathrm{vol}}(\det \boldsymbol{F})[\boldsymbol{H}] &= (\det \boldsymbol{F} - 1)\left(\frac{1}{6}\boldsymbol{H} : (\boldsymbol{F} \times \boldsymbol{F}) + \frac{1}{3}\boldsymbol{F} : (\boldsymbol{H} \times \boldsymbol{F})\right) \\ &= \frac{1}{2}(\det \boldsymbol{F} - 1)\,\boldsymbol{H} : (\boldsymbol{F} \times \boldsymbol{F}) = (\det \boldsymbol{F} - 1)\,\mathit{Cof}(\boldsymbol{F}) : \boldsymbol{H}. \end{aligned}$$